Article

Structural Analysis, Phase Stability, Electronic Band Structures, and Electric Transport Types of $(Bi_2)_m(Bi_2Te_3)_n$ by Density Functional Theory Calculations

Sungjin Park *[ID], Byungki Ryu [ID] and SuDong Park

Energy Conversion Research Center, Korea Electrotechnology Research Institute (KERI), Changwon 51543, Korea; byungkiryu@keri.re.kr (B.R.); john@keri.re.kr (S.P.)
* Correspondence: sjinpark@keri.re.kr; Tel.: +82-55-280-2549; Fax: +82-55-280-1590

Abstract: Thermoelectric power generation is a promising candidate for automobile energy harvesting technologies because it is eco-friendly and durable owing to direct power conversion from automobile waste heat. Because Bi−Te systems are well-known thermoelectric materials, research on $(Bi_2)_m(Bi_2Te_3)_n$ homologous series can aid the development of efficient thermoelectric materials. However, to the best of our knowledge, $(Bi_2)_m(Bi_2Te_3)_n$ has been studied through experimental synthesis and measurements only. Therefore, we performed density functional theory calculations of nine members of $(Bi_2)_m(Bi_2Te_3)_n$ to investigate their structure, phase stability, and electronic band structures. From our calculations, although the total energies of all nine phases are slightly higher than their convex hulls, they can be metastable owing to their very small energy differences. The electric transport types of $(Bi_2)_m(Bi_2Te_3)_n$ do not change regardless of the exchange–correlation functionals, which cause tiny changes in the atomic structures, phase stabilities, and band structures. Additionally, only two phases (Bi_8Te_9, BiTe) became semimetallic or semiconducting depending on whether spin–orbit interactions were included in our calculations, and the electric transport types of the other phases were unchanged. As a result, it is expected that Bi_2Te_3, Bi_8Te_9, and BiTe are candidates for thermoelectric materials for automobile energy harvesting technologies because they are semiconducting.

Keywords: energy harvesting; automobile; $(Bi_2)_m(Bi_2Te_3)_n$ homologous series; mixing energy; phase stability; electronic band structures; electric transport types; density functional theory calculations

1. Introduction

Gasoline and hybrid electric vehicles cause waste heat energy to be released into the environment because of inefficient conversion of approximately 25% from chemical energy into mechanical energy through exhaust gases and coolants [1–3]. Automobile energy harvesting technology has attracted significant attention from the automobile industry to reduce the fuel consumption of vehicles [3,4]. In addition, automobile waste heat recovery has been intensively investigated to alleviate global warming and improve the efficiency of vehicles [1,2,4–9]. Meanwhile, thermoelectric generators are eco-friendly and durable owing to direct power conversion into electricity from automobile waste heat [1,2,4–6,8,9]. As a result, energy harvesting using thermoelectric generators in automobiles has been considered as an option to recover automobile waste heat.

The Seebeck effect and conversion efficiency are important in thermoelectric energy harvesting technology. The thermoelectric dimensionless figure of merit (ZT) is defined as $ZT = \alpha^2 \sigma T / \kappa$, where α is the Seebeck coefficient, σ is the electrical conductivity, κ is the thermal conductivity, and T is the absolute temperature [9,10]. The thermoelectric conversion efficiency (η) is defined as $\eta = P_{out}/Q_h$, where P_{out} is the electric output power and Q_h is the heat input [9,10]. Many researchers have investigated thermoelectric materials with high ZT and η for applications in thermoelectric energy harvesting [6,11–13].

Meanwhile, $(Bi_2)_m(Bi_2Te_3)_n$ homologous series have been investigated as layer-stacked structures consisting of Bi bilayers and Bi_2Te_3 quintuple layers. In addition, they have been synthesised experimentally and their structural (lattice parameters, volume, etc.) and thermoelectric properties (resistivity, Seebeck coefficient, etc.) have been measured [14–18]. In particular, it has been demonstrated that $(Bi_2)_m(Bi_2Te_3)_n$ exhibits intrinsically low lattice thermal conductivity due to chemical bond softening and lattice anharmonicity [18]. However, to the best of our knowledge, no research has been conducted on the structural analysis and electronic band structures of $(Bi_2)_m(Bi_2Te_3)_n$.

First-principles density functional theory calculations of the $(Bi_2)_m(Bi_2Te_3)_n$ homologous series were performed to investigate their internal structures, phase stability from mixing energies, and electronic band structures. From the structural analysis, it was found that exchange–correlation functionals affect both the intralayer thickness and interlayer distances of $(Bi_2)_m(Bi_2Te_3)_n$. Further, it was revealed that the $(Bi_2)_m(Bi_2Te_3)_n$ homologous series can be metastable from a comparison between their layer mixing energies and the convex hull. In addition, the energy gaps and band edges of $(Bi_2)_m(Bi_2Te_3)_n$ were determined from electronic band structure calculations. Consequently, electric transport types were obtained, and the $(Bi_2)_m(Bi_2Te_3)_n$ considered here were semimetallic or semiconducting. In particular, Bi_2Te_3, Bi_8Te_9, and BiTe among the $(Bi_2)_m(Bi_2Te_3)_n$ homologous series were semiconducting. Therefore, Bi_2Te_3, Bi_8Te_9, and BiTe are expected to be feasible thermoelectric materials for applications in automobile energy harvesting.

2. Methods and Calculations Details

First-principles density functional theory (DFT) [19,20] calculations were performed. The DFT calculations were implemented using the Vienna Ab initio simulation package [21–23]. A plane-wave basis set with an energy cut-off of 300 eV was used with the Perdew–Burke–Ernzerhof (PBE) exchange correlational functional (E_{xc}) [24], and local density approximation (LDA) [23] and projector augmented wave (PAW) pseudopotentials [25,26] were used: PAW_PBE Bi_d_GW 14Apr2014, PAW_PBE Te_GW 22Mar2012 for PBE and PAW Bi_d_GW 14Apr2014, PAW Te_GW 22Mar2012 for LDA. A $12 \times 12 \times k_3$ Γ-centered k-point mesh grid was used to sample the k-point in the Brillouin zone, where k_3 is a subdivision of the third direction along the third reciprocal lattice vector. To consider the relativistic correction of heavy elements such as Bi and Te, the spin–orbit interaction (SOI) was employed [27–29].

The structures of the $(Bi_2)_m(Bi_2Te_3)_n$ homologous series considered here were obtained from Bos' research [14]. Their end members were semiconducting Bi_2Te_3 and semimetallic Bi_2; nine members of the series were studied: Bi_2Te_3, Bi_4Te_5, Bi_6Te_7, Bi_8Te_9, BiTe, Bi_4Te_3, Bi_2Te, Bi_7Te_3, and Bi_2. Here, the ratio of Bi_2 to Bi_2Te_3 increased in the following order from Bi_2Te_3 to Bi_2 as the ratio of m to n: 0:3, 1:5, 2:7, 3:9, 1:2, 3:3, 2:1, 15:6, and 3:0 (see Figure 1). In the figure, the side view shows the atomic structure viewed from the *a*-axis direction, and the top view shows the atomic structure viewed from the *c*-axis direction. The purple spheres represent Bi atoms and the gold spheres are Te atoms. The red blocks are the Bi bilayers (BLs) and the blue blocks the Bi_2Te_3 quintuple layers (QLs). The lattice parameters of the *a*-axis and the *c*-axis in the hexagonal supercells were obtained from previous experimental studies of $(Bi_2)_m(Bi_2Te_3)_n$ materials [14–17] (see Table 1). In particular, we referred to the layer-stacking method of BL and QL in Bos' study [14]; for convenient calculations, the different stacking methods of BL and QL were not considered. Furthermore, the optimised atomic structure of each material of $(Bi_2)_m(Bi_2Te_3)_n$ was obtained while lowering the total force acting on each atom below 10^{-3} eV/Å, where the initial atomic structure had fixed lattice parameters with all the atoms arrayed equidistantly in the direction of the *c*-axis.
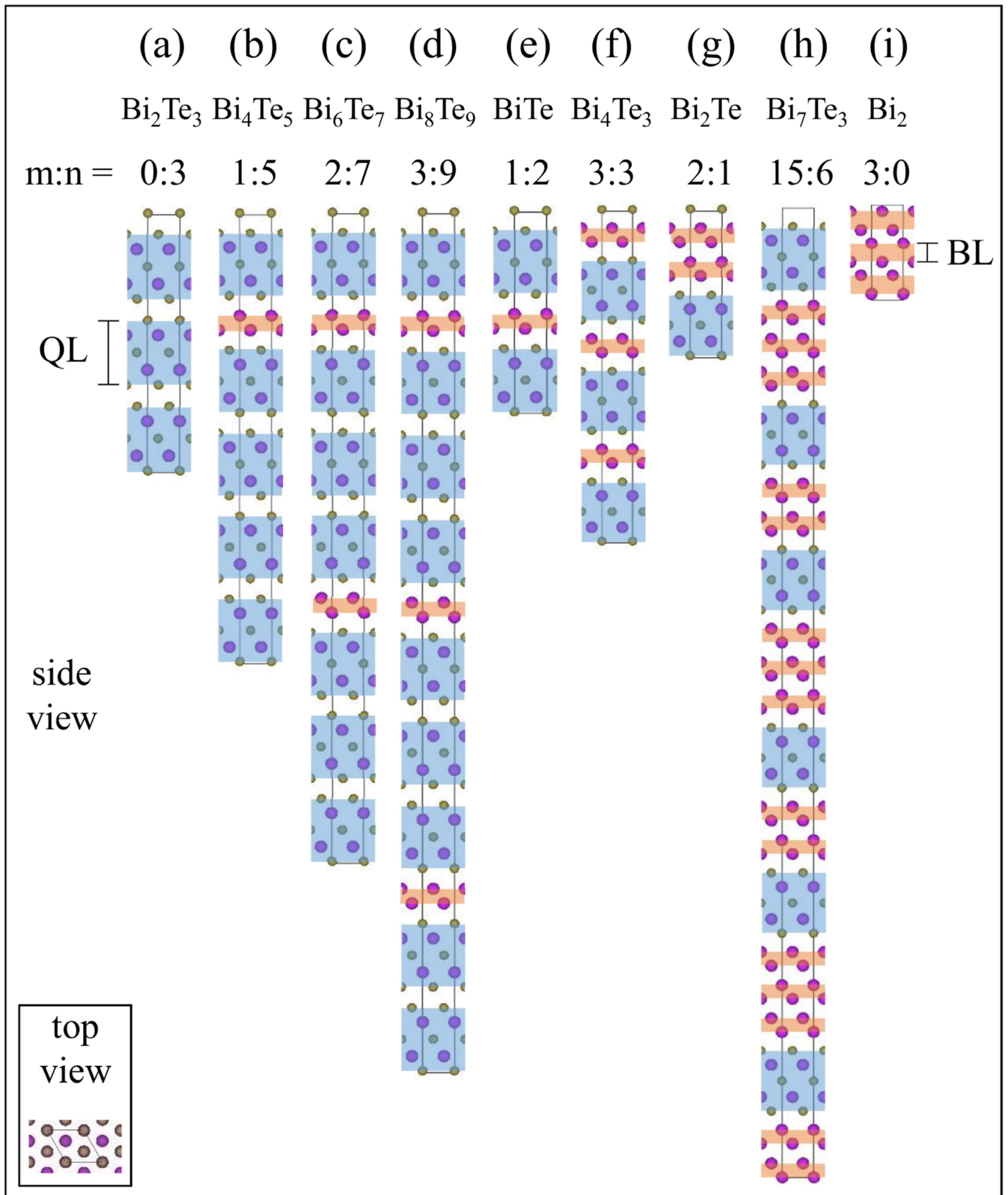
Figure 1. Atomic structures of hexagonal $(Bi_2)_m(Bi_2Te_3)_n$: (**a**) Bi_2Te_3, (**b**) Bi_4Te_5, (**c**) Bi_6Te_7, (**d**) Bi_8Te_9, (**e**) BiTe, (**f**) Bi_4Te_3, (**g**) Bi_2Te, (**h**) Bi_7Te_3, and (**i**) Bi_2. The violet and gold balls indicate Bi and Te, respectively. The red and blue blocks display the Bi_2 bilayer (BL) and Bi_2Te_3 quintuple layer (QL), respectively. The side and top view indicate the atomic structure seen from the vector direction of $\vec{a}$ and $\vec{c}$ in each respective $(Bi_2)_m(Bi_2Te_3)_n$ lattice.

Table 1. Phase properties, structural parameters, intralayer thickness, and interlayer distance of $(Bi_2)_m(Bi_2Te_3)_n$ homologous series depending on the E_{xc} used for our calculations.

	Chemical Formula		Bi_2Te_3	Bi_4Te_5	Bi_6Te_7	Bi_8Te_9	BiTe	Bi_4Te_3	Bi_2Te	Bi_7Te_3	Bi_2
Phase properties	Hexagonal compositions		Bi_6Te_9	$Bi_{12}Te_{15}$	$Bi_{18}Te_{21}$	$Bi_{24}Te_{27}$	Bi_6Te_6	$Bi_{12}Te_9$	Bi_6Te_3	$Bi_{42}Te_{18}$	Bi_6
	N_{BL} : N_{QL}		0:3	1:5	2:7	3:9	1:2	3:3	2:1	15:6	3:0
	$N_{BL}/(N_{BL} + N_{QL})$		0	0.167	0.222	0.250	0.333	0.500	0.667	0.714	1
Structural parameters	Volume/N_{Atom} (Å³)		33.892	33.974	33.986	34.015	33.887	34.224	35.093	34.352	35.383
	a_{Hex} (Å)		4.388	4.415	4.424	4.410	4.423	4.451	4.490	4.472	4.546
	c_{Hex} (Å)		30.488	54.330	78.200	103.000	24.002	41.890	18.090	119.000	11.862
	c_{Hex}/N_{Atom} (Å)		2.033	2.012	2.005	2.020	2.000	1.995	2.010	1.983	1.977
PBE — w/o SOI	Intralayer thickness (Å)	BL	-	1.697	1.693	1.701	1.692	1.681	1.671	1.674	1.977
		QL	7.529	7.472	7.453	7.492	7.449	7.415	7.390	7.358	-
	Interlayer distance (Å)	BL-BL	-	-	-	-	-	-	2.464	2.375	1.977
		BL-QL	-	2.436	2.428	2.453	2.421	2.434	2.447	2.363	-
		QL-QL	2.634	2.600	2.586	2.626	2.570	-	-	-	-
PBE — w/ SOI	Intralayer thickness (Å)	BL	-	1.758	1.753	1.762	1.748	1.729	1.704	1.702	1.977
		QL	7.623	7.560	7.538	7.579	7.525	7.480	7.454	7.409	-
	Interlayer distance (Å)	BL-BL	-	-	-	-	-	-	2.468	2.375	1.977
		BL-QL	-	2.412	2.400	2.423	2.386	2.377	2.380	2.303	-
		QL-QL	2.539	2.488	2.465	2.494	2.433	-	-	-	-
LDA — w/o SOI	Intralayer thickness (Å)	BL	-	1.661	1.657	1.66	1.657	1.645	1.632	1.638	1.977
		QL	7.454	7.403	7.384	7.419	7.383	7.346	7.310	7.291	-
	Interlayer distance (Å)	BL-BL	-	-	-	-	-	-	2.525	2.426	1.977
		BL-QL	-	2.474	2.469	2.492	2.467	2.486	2.495	2.404	-
		QL-QL	2.709	2.677	2.663	2.714	2.645	-	-	-	-
LDA — w/ SOI	Intralayer thickness (Å)	BL	-	1.718	1.714	1.722	1.710	1.693	1.661	1.661	1.977
		QL	7.565	7.509	7.489	7.526	7.476	7.421	7.381	7.345	-
	Interlayer distance (Å)	BL-BL	-	-	-	-	-	-	2.549	2.439	1.977
		BL-QL	-	2.466	2.450	2.476	2.434	2.425	2.419	2.338	-
		QL-QL	2.598	2.534	2.510	2.540	2.471	-	-	-	-

In the atomic structure of the $(Bi_2)_m(Bi_2Te_3)_n$ homologous series, the number of BLs or QLs was defined as N_{BL} or N_{QL}, respectively. The total number of atoms in each phase was defined as N_{Atom}. Furthermore, the average thickness of BL or QL was defined as the intralayer thickness of BL or QL. Additionally, the average distance between BL and BL, BL and QL, or QL and QL was defined as the interlayer distances of BL−BL, BL−QL, or QL−QL, respectively (see Table 1 and Figure 1).

To investigate the relative stability of $(Bi_2)_m(Bi_2Te_3)_n$ when mixing BL and QL, the layer mixing energy of each phase per atom was defined as

$$E_{Mixing} = \frac{E_{Total}^{(Bi_2)_m(Bi_2Te_3)_n} - m\, E_{Total}^{Bi_2} - n\, E_{Total}^{Bi_2Te_3}}{N_{atom}} \qquad (1)$$

where $E_{Total}^{(Bi_2)_m(Bi_2Te_3)_n}$, $E_{Total}^{Bi_2}$, and $E_{Total}^{Bi_2Te_3}$ are the total energies of $(Bi_2)_m(Bi_2Te_3)_n$, Bi_2, and Bi_2Te_3, respectively. Note that E_{Mixing} is normalised by the total atomic number in the supercell (N_{atom}) to reflect only the structural differences between the $(Bi_2)_m(Bi_2Te_3)_n$ phases. In addition, note that only zero-temperature E_{Mixing} is displayed here because the temperature dependence of E_{Mixing} is not of interest.

Our electronic band structures with density of states (DOS) were generated using pymatgen [30] based on our DFT calculations. In our band calculations, the electronic band structures of the full k-point path (Γ−M−K−Γ−A−L−H−A, L−M, K−H) were obtained with 51 mesh grids in the first Brillouin zone of hexagonal lattices. From this, it was found that all the valence band maximum (VBM) and conduction band minimum (CBM) of the $(Bi_2)_m(Bi_2Te_3)_n$ considered in this study were located in the k-point path of K−Γ−M or L−A−H for our calculation setting: K (0.333, 0.333, 0), Γ (0, 0, 0), M (0.5, 0, 0), L (0.5, 0, 0.5), A (0, 0, 0.5), H (0.333, 0.333, 0.5). Consequently, only electronic band structures in K−Γ−M and L−A−H are presented for the E_{xc} used in our calculations. In addition,

our electronic band structures were projected onto atomic elements (Bi: blue, Te: red), except for Bi_2, and our DOS is projected onto electronic orbitals (s: blue, p: red, d: green, f: violet). For the electronic band topology of $(Bi_2)_m(Bi_2Te_3)_n$ phases, the direct bandgap was defined as E_{gap}^d (the minimum of the difference between CBM and VBM at the same k-point) and the indirect bandgap as E_{gap}^i (the difference between CBM and VBM). Electric types were defined to determine the electric transport characteristics of $(Bi_2)_m(Bi_2Te_3)_n$: semiconductors if both E_{gap}^d and E_{gap}^i were positive, semimetals if E_{gap}^d was positive and E_{gap}^i negative, and metals if both E_{gap}^d and E_{gap}^i were negative.

3. Results and Discussions

Table 1 shows the chemical formula, hexagonal composition, ratio between the number of BLs and QL ($N_{BL}:N_{QL}$), ratio between N_{BL} and the total number of layers ($N_{BL}/(N_{BL} + N_{QL})$), lattice volume per atom (Volume/N_{Atom}), lattice constants in a hexagonal supercell (a_{Hex}, c_{Hex}), c_{Hex} per atom (c_{Hex}/N_{Atom}), average intralayer thickness, and average interlayer distance depending on E_{xc} with (w/) or without (w/o) SOI used in our calculations. Note that N_{Atom} is the same as the total number of layers in each phase because our unit cells contain only a single atom on one layer. Additionally, note that N_{BL}/N_{Atom} increases from 0 to 1 as the proportion of BL increases from Bi_2Te_3 to Bi_2. In addition, for each $(Bi_2)_m(Bi_2Te_3)_n$, the lattice parameters in the a vector direction were 4.388–4.546 Å, the lattice parameters in the c vector direction were 11.862–119 Å, and the volume per atom (Volume/N_{Atom}) was 33.887–35.383 Å^3. The average lattice parameters along the *c*-axis with respect to the number of layers were 1.977–2.033 Å.

The intralayer thicknesses of the atomic structure of $(Bi_2)_m(Bi_2Te_3)_n$ obtained through the DFT calculations were investigated, except for Bi_2 and Bi_2Te_3. Based on the intralayer thickness without considering the SOI, the rate of increase of each intralayer thickness was calculated depending on whether or not SOI was considered. Regardless of the type of Exc used, the intralayer thickness with respect to SOI increased significantly compared to the thickness without considering SOI. In the case of PBE, the intralayer thicknesses of BL and QL for $(Bi_2)_m(Bi_2Te_3)_n$ were 1.697 Å and 7.472 Å for Bi_4Te_5, 1.693 Å and 7.453 Å for Bi_6Te_7, 1.701 Å and 7.492 Å for Bi_8Te_9, 1.692 Å and 7.449 Å for $BiTe$, 1.681 Å and 7.415 Å for Bi_4Te_3, 1.671 Å and 7.390 Å for Bi_2Te, and 1.674 Å and 7.358 Å, Bi_7Te_3, respectively. In PBE with SOI, compared to PBE, the thickness of BL increases by 1.64–3.63% and the thickness of QL also increases by 0.69–1.25% depending on their atomic structures. In LDA, the intralayer thicknesses of BL and QL for $(Bi_2)_m(Bi_2Te_3)_n$ were 1.661 Å and 7.403 Å for Bi_4Te_3, 1.657 Å and 7.384 Å for Bi_6Te_7, 1.664 Å and 7.419 Å for Bi_8Te_9, 1.657 Å and 7.383 Å for $BiTe$, 1.645 Å and 7.346 Å for Bi_4Te_3, 1.632 Å and 7.310 Å for Bi_2Te, and 1.638 Å and 7.291 Å for Bi_7Te_3, respectively. In LDA with SOI, compared to LDA, the thickness of BL increases by 1.40–3.51% and that of QL by 0.75–1.49%. Consequently, all increase rates of the intralayer thickness have positive values regardless of the intralayer type and the thickness of BL increases by more than 1.8 times of QL if SOI is considered, regardless of the phase of $(Bi_2)_m(Bi_2Te_3)_n$. In addition, considering the SOI, the intralayer thickness of BL for PBE increases more than that of BL for LDA, although that of QL for PBE increases less than that of QL for LDA. This indicates that the E_{xc} of PBE (PBE w/o or w/SOI) overestimates the intralayer thickness of BL by more than 2% compared to that of LDA (LDA w/o or w/SOI). Furthermore, this indicates that the intralayer thickness of QL is overestimated by less than 1.1% by PBE compared with LDA. Thus, this shows that LDA underestimates the distances between adjacent atoms along the *c*-axis in the intralayers compared with PBE.

The interlayer distances of $(Bi_2)_m(Bi_2Te_3)_n$ were also analysed. Depending on the layer stacking in $(Bi_2)_m(Bi_2Te_3)_n$, there were BL–BL, BL–QL, and QL–QL interlayer distances; BL–BL interfaces were only observed in Bi_2Te and Bi_7Te_3; BL–QL interfaces were present in the remaining phases except for Bi_2Te_3 and Bi_2; and QL–QL interfaces were observed in Bi_2Te_3, Bi_4Te_3, Bi_6Te_7, Bi_8Te_9, and $BiTe$. PBE (LDA) calculation gives the interlayer distances, as shown in Table 1. For BL–BL in PBE, the interlayer distances are almost unaffected by considering SOI owing to their increase of less than 1%. However, for BL–

QL, when considering SOI, their interlayer distances decrease by more than 1.3% when $N_{BL}/N_{Layer} \geq 0.333$, although they remain almost constant for the other phases owing to their changes of less than 1.3%. For QL–QL, owing to SOI, their interlayer distances were reduced by more than 3.5%, unlike BL–BL and BL–QL; in particular, LDA decreased the interlayer distances of QL–QL by more than 1% compared to PBE, except for Bi_2Te_3. Thus, employing SOI in our calculations caused greater changes in the interlayer distances of QL–QL than those of the other interfaces. This revealed that PBE underestimated the interlayer distances compared to LDA: over 2% for BL–BL, over 1.5% for BL–QL, and over 1.5% for QL–QL.

Figure 2 shows the layer mixing energies (E_{Mixing}) of $(Bi_2)_m(Bi_2Te_3)_n$ as a function of $N_{BL}/N_{Layer} = N_{BL}/(N_{BL} + N_{QL})$. Because there is no layer mixing between QL and BL in Bi_2Te_3 and Bi_2, their E_{Mixing} is zero. Figure 2a shows the convex hull and E_{Mxing} in PBE and PBE + SOI. In PBE + SOI, E_{Mxing} exhibits a convex hull through Bi_2Te_3–Bi_2Te–Bi_2. Compared to the convex hull, the E_{Mixing} differs by 0.0017 eV/atom for Bi_4Te_5, 0.0022 eV/atom for Bi_6Te_7, 0.0025 eV/atom for Bi_8Te_9, 0.0045 eV/atom for BiTe, 0.0003 eV/atom for Bi_4Te_3, and 0.0027 eV/atom for Bi_7Te_3, respectively. The E_{Mixing} of PBE is similar to that of PBE + SOI with a few exceptions: in PBE, the difference between the convex hull and E_{Mxing} was, on average, ~1.7 times larger than that in PBE + SOI, except for Bi_4Te_3 and Bi_7Te_3, whereas in PBE, the differences of Bi_4Te_3 and Bi_7Te_3 were ~13.6 and ~0.4 times larger than those in PBE + SOI, respectively. In fact, the differences are less than 0.0045 eV/atom, except for that of BiTe in PBE (0.0070 eV/atom). This indicates that the $(Bi_2)_m(Bi_2Te_3)_n$ phases can exist energetically because their E_{Mixing} is very close to their convex hulls. Meanwhile, considering the SOI, overall E_{Mixing}, on average, decreased by 0.0095 eV; the maximum decrease was 0.014 eV for Bi_4Te_3, and the minimum was 0.0048 eV for Bi_4Te_5. This indicates that E_{Mixing} was overestimated by the PBE calculations with SOI than those without SOI. On the other hand, Figure 2b exhibits a convex hull and E_{Mixing} in LDA and LDA + SOI. Note that the convex hulls of LDA functionals (LDA and LDA + SOI) have different shapes from those of PBE functionals (PBE and PBE + SOI). In particular, the convex hull of LDA passes through Bi_2Te_3–Bi_7Te_3–Bi_2 and that of LDA + SOI through Bi_2Te_3–Bi_4Te_3–Bi_7Te_3–Bi_2. Compared to the convex hull in LDA + SOI, E_{Mixing} differs by 0.0019 eV for Bi_4Te_5, 0.0021 eV for Bi_6Te_7, 0.0027 eV for Bi_8Te_9, 0.0006 eV for BiTe, and 0.0067 eV for Bi_2Te. In LDA, the difference between the convex hull and E_{Mxing} was, on average, about two times larger than that in LDA + SOI except for Bi_8Te_9 and Bi_4Te_3; in particular, that of BiTe was ~3.8 times larger. The differences were less than 0.0035 eV, except for those of Bi_2Te in LDA (0.0098 eV) and LDA + SOI (0.0067 eV). In addition, considering the SOI, overall E_{Mixing}, on average, decreased by 0.0091 eV; the maximum decrease was 0.0135 eV for Bi_4Te_3, and the minimum was 0.0046 eV for Bi_4Te_5. Thus, this demonstrates that LDA overestimates the phase stabilities of $(Bi_2)_m(Bi_2Te_3)_n$ compared to PBE.

Figures 3–6 show the electronic band structures with their DOS for $(Bi_2)_m(Bi_2Te_3)_n$ obtained using PBE or LDA calculations, without and with SOI, respectively. All the DOS comprised small components of s- and d-orbital as well as that of large p-orbital in the whole energy range of electrons. It is clear that the orbitals of Bi 6p and Te 5p mainly contribute to the dominant p-orbital component. Note that the shapes of the electronic band structures are more complicated than the N_{Atom} increases due to supercell calculations. Meanwhile, for the convenience of band structure analysis, the VBM and CBM of each phase were used and the band topology near the band edge (VBM, CBM) was investigated. The E_{gap}^d and E_{gap}^i of all the phases and their reciprocal positions were obtained. From this, the electrical transport types (semiconductor, semimetal, or metal) of all the phases were investigated. The electric transport types with the band structures using PBE and LDA are summarised in Tables 2 and 3, respectively.
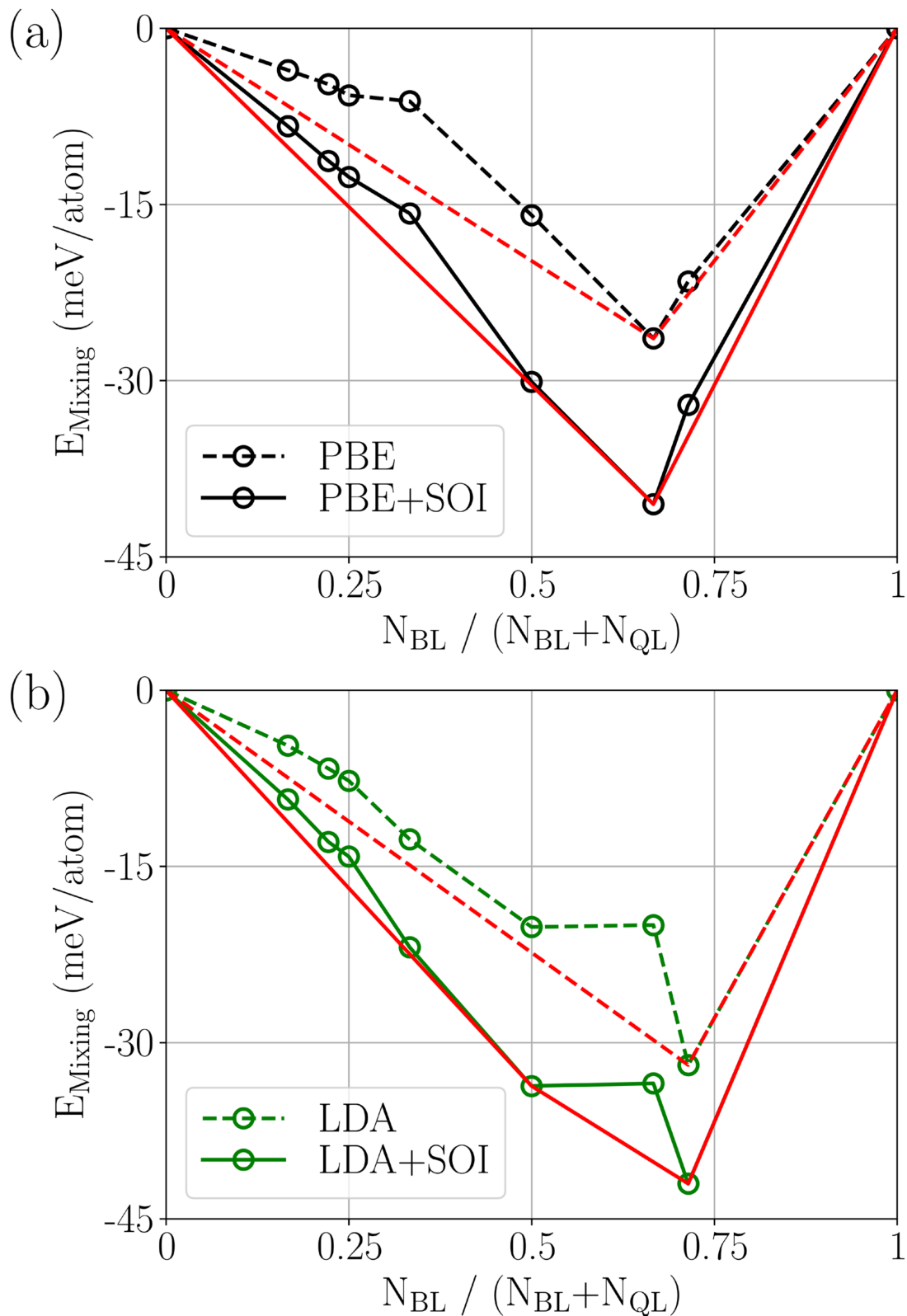
Figure 2. Layer mixing energy (E_{Mixing}) of $(Bi_2)_m(Bi_2Te_3)_n$ for (**a**) PBE and (**b**) LDA as a function of $N_{BL}/(N_{BL} + N_{QL})$. The black dashed line shows E_{Mixing} for PBE, and the black line represents the E_{Mixing} for PBE with SOI (PBE + SOI), where the red solid and dashed lines indicate a convex hull of E_{Mixing} for PBE and PBE + SOI, respectively. The green dashed line displays E_{Mixing} for LDA, and the green dashed line represents E_{Mixing} for LDA with SOI (LDA + SOI), where the red solid and dashed lines indicate the convex hull of E_{Mixing} for LDA and LDA + SOI.
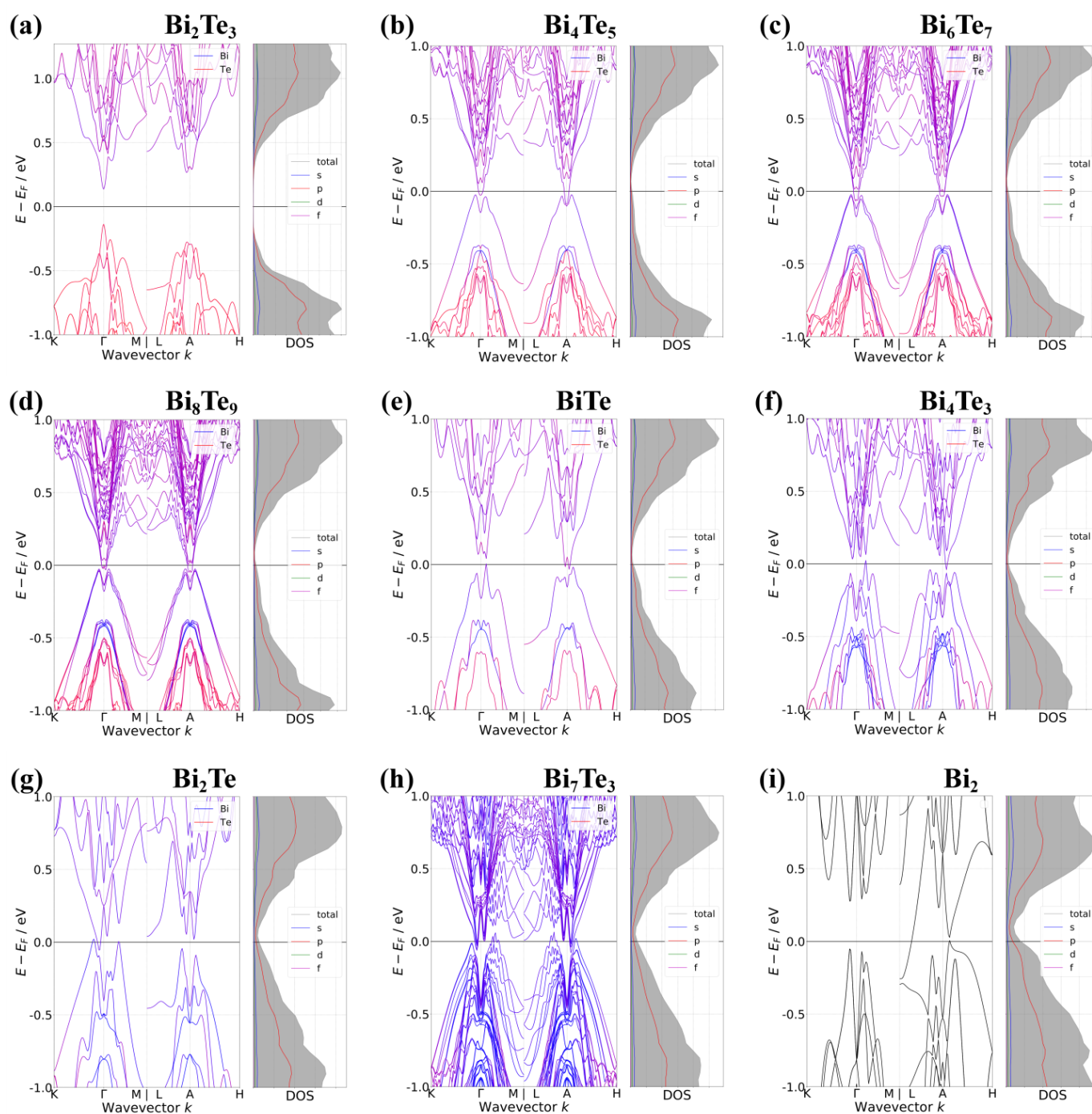
Figure 3. Electronic band structures with density of states along the k-point paths of M−Γ−K and L−A−H in hexagonal $(Bi_2)_m(Bi_2Te_3)_n$: (**a**) Bi_2Te_3, (**b**) Bi_4Te_5, (**c**) Bi_6Te_7, (**d**) Bi_8Te_9, (**e**) BiTe, (**f**) Bi_4Te_3, (**g**) Bi_2Te, (**h**) Bi_7Te_3, and (**i**) Bi_2. All band structures were obtained using DFT calculations with PBE.

Figure 4. Electronic band structures with the density of states along the k-point paths of M−Γ−K and L−A−H in hexagonal $(Bi_2)_m(Bi_2Te_3)_n$: (**a**) Bi_2Te_3, (**b**) Bi_4Te_5, (**c**) Bi_6Te_7, (**d**) Bi_8Te_9, (**e**) BiTe, (**f**) Bi_4Te_3, (**g**) Bi_2Te, (**h**) Bi_7Te_3, and (**i**) Bi_2. All band structures were obtained by using DFT calculations with PBE including SOI.

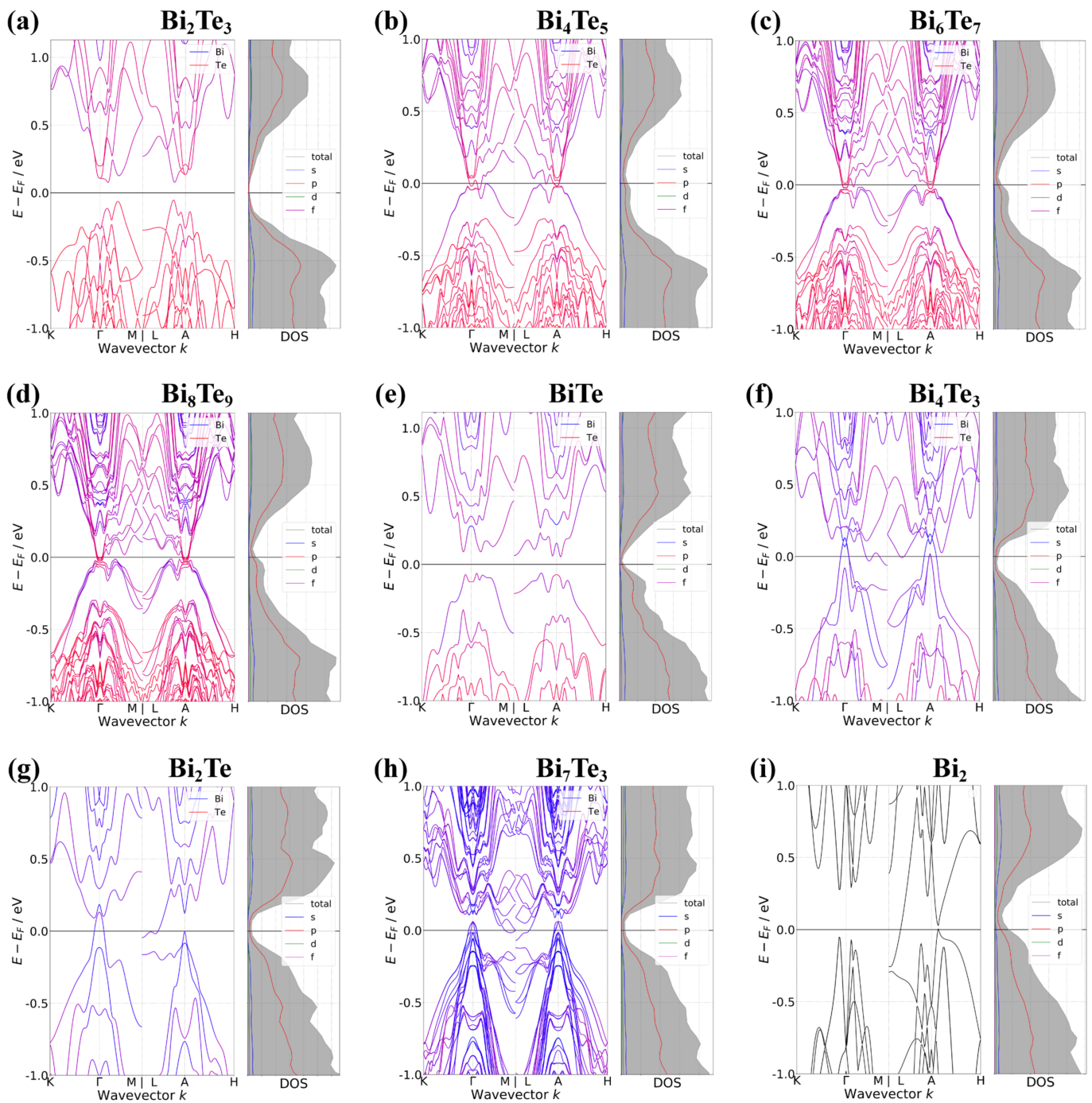**Figure 5.** Electronic band structures with density of states along the k-point path of M−Γ−K and L−A−H in hexagonal $(Bi_2)_m(Bi_2Te_3)_n$: (**a**) Bi_2Te_3, (**b**) Bi_4Te_5, (**c**) Bi_6Te_7, (**d**) Bi_8Te_9, (**e**) BiTe, (**f**) Bi_4Te_3, (**g**) Bi_2Te, (**h**) Bi_7Te_3, and (**i**) Bi_2. All band structures were obtained by using DFT calculations with LDA.

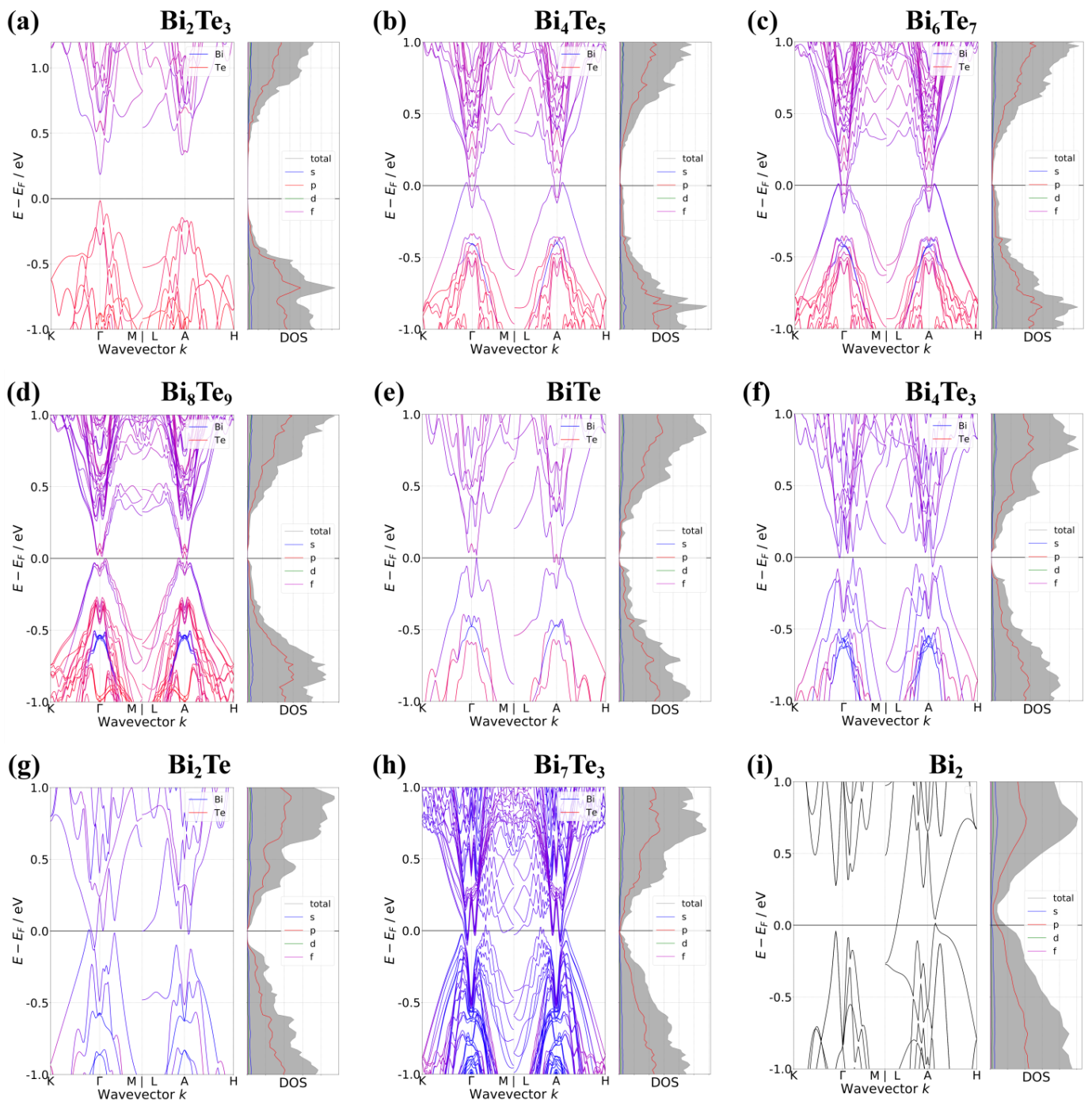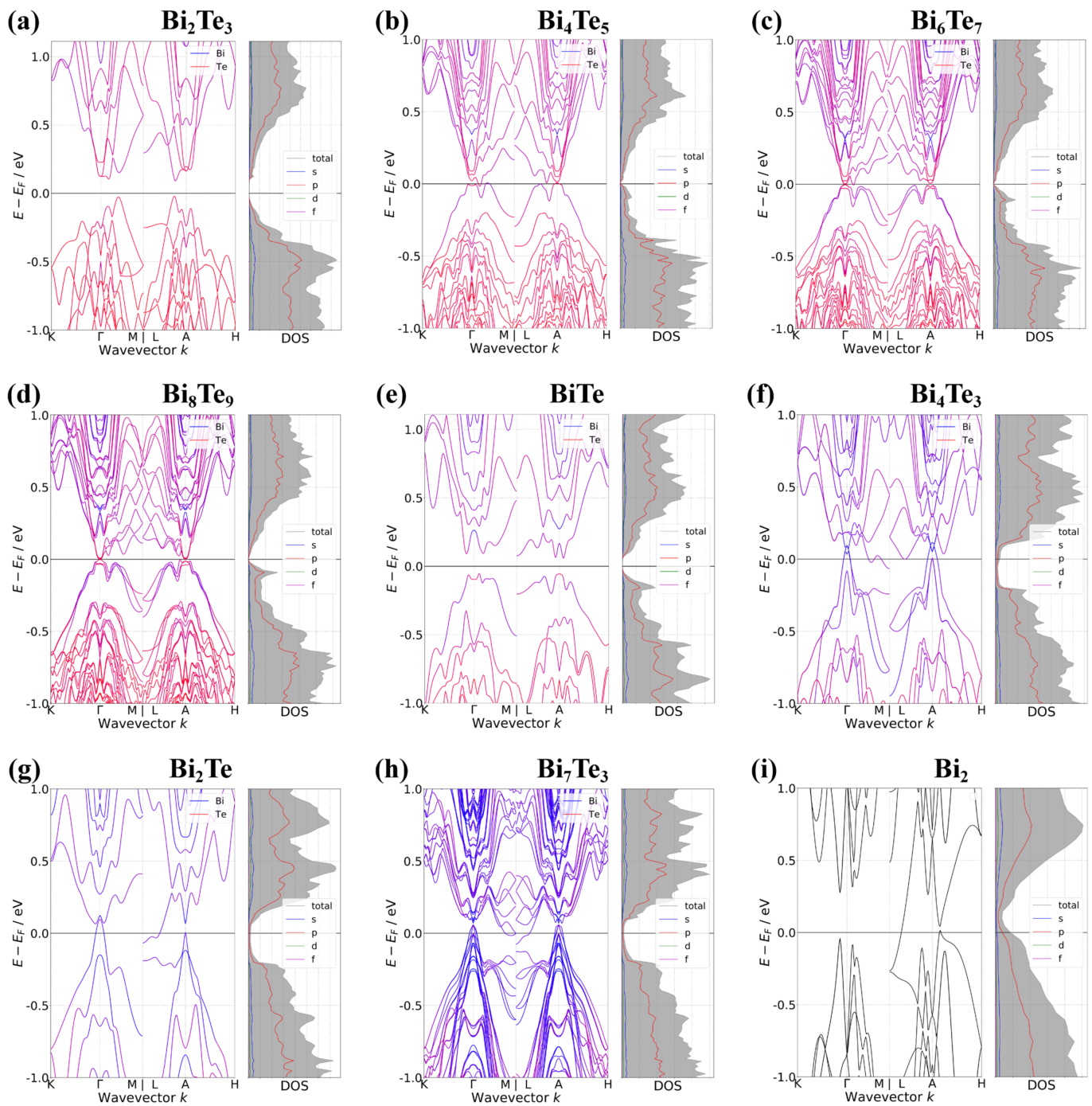**Figure 6.** Electronic band structures with density of states along the k-point path of M−Γ−K and L−A−H in hexagonal $(Bi_2)_m(Bi_2Te_3)_n$: (**a**) Bi_2Te_3, (**b**) Bi_4Te_5, (**c**) Bi_6Te_7, (**d**) Bi_8Te_9, (**e**) BiTe, (**f**) Bi_4Te_3, (**g**) Bi_2Te, (**h**) Bi_7Te_3, and (**i**) Bi_2. All band structures were obtained by using DFT calculations with LDA including SOI.

Table 2. Determination of electric transport types (Type) of $(Bi_2)_m(Bi_2Te_3)_n$ from the energy gap in electronic band structure depending on the exclusion (X) and inclusion (O) of SOI using the E_{xc} of PBE. E_{VBM} and E_{CBM} are the energy of VBM and CBM relative to the Fermi level of each $(Bi_2)_m(Bi_2Te_3)_n$, respectively. E_{gap}^i and E_{gap}^d are the indirect and direct energy gaps, respectively. k_{VBM}, k_{CBM}, and k_{gap}^d are reciprocal positions of VBM, CBM, and E_{gap}^d in the first Brillouin zone, respectively. SC and SM represent semiconductors and semimetals, respectively.

E_{xc}	Phase	SOI	E_{VBM}	k_{VBM}	E_{CBM}	k_{CBM}	E_{gap}^i	E_{gap}^d	k_{gap}^d	Type
PBE	Bi_2Te_3	X	−0.136	0.000 0.000 0.000	0.136	0.000 0.000 0.000	0.272	0.272	0.000 0.000 0.000	SC
		O	−0.061	0.140 0.000 0.500	0.068	0.090 0.000 0.000	0.129	0.135	0.130 0.000 0.500	SC
	Bi_4Te_5	X	0.006	0.033 0.033 0.500	−0.059	0.000 0.000 0.500	−0.065	0.005	0.010 0.000 0.500	SM
		O	0.012	0.170 0.000 0.000	−0.035	0.090 0.000 0.000	−0.047	0.004	0.010 0.000 0.500	SM
	Bi_6Te_7	X	0.002	0.033 0.033 0.000	−0.043	0.007 0.007 0.000	−0.045	0.029	0.020 0.000 0.000	SM
		O	0.006	0.180 0.000 0.500	−0.018	0.000 0.000 0.500	−0.024	0.008	0.020 0.000 0.000	SM
	Bi_8Te_9	X	−0.004	0.033 0.033 0.500	−0.030	0.007 0.007 0.500	−0.026	0.027	0.020 0.000 0.500	SM
		O	0.001	0.170 0.000 0.500	−0.019	0.000 0.000 0.500	−0.020	0.001	0.000 0.000 0.500	SM
	BiTe	X	0.017	0.060 0.000 0.000	−0.023	0.013 0.013 0.500	−0.040	0.035	0.060 0.000 0.000	SM
		O	−0.064	0.180 0.000 0.500	0.053	0.027 0.027 0.500	0.117	0.152	0.040 0.000 0.500	SC
	Bi_4Te_3	X	0.030	0.110 0.000 0.000	−0.036	0.027 0.027 0.500	−0.066	0.021	0.027 0.027 0.500	SM
		O	0.108	0.000 0.000 0.000	−0.084	0.500 0.000 0.000	−0.192	0.001	0.020 0.000 0.000	SM
	Bi_2Te	X	0.025	0.067 0.067 0.000	−0.051	0.033 0.033 0.000	−0.076	0.038	0.033 0.033 0.000	SM
		O	0.138	0.000 0.000 0.000	−0.041	0.500 0.000 0.500	−0.179	0.030	0.030 0.000 0.000	SM
	Bi_7Te_3	X	0.077	0.150 0.000 0.500	−0.068	0.027 0.027 0.500	−0.145	0.021	0.027 0.027 0.500	SM
		O	0.041	0.000 0.000 0.500	−0.093	0.500 0.000 0.500	−0.134	0.025	0.020 0.020 0.500	SM
	Bi_2	X	0.066	0.047 0.047 0.500	−0.197	0.480 0.000 0.500	−0.263	0.020	0.047 0.047 0.500	SM
		O	0.113	0.000 0.000 0.500	−0.048	0.500 0.000 0.500	−0.161	0.079	0.500 0.000 0.500	SM

Table 3. Determination of electric transport type (Type) of $(Bi_2)_m(Bi_2Te_3)_n$ from the energy gap in the electronic band structure depending on the exclusion (X) and inclusion (O) of SOI using the E_{xc} of LDA. E_{VBM} and E_{CBM} are the energy of VBM and CBM relative to the Fermi level of each $(Bi_2)_m(Bi_2Te_3)_n$, respectively. E_{gap}^i and E_{gap}^d are the indirect and direct energy gaps, respectively. k_{VBM}, k_{CBM}, and k_{gap}^d are reciprocal positions of VBM, CBM, and E_{gap}^d in the first Brillouin zone, respectively. SC and SM represent semiconductors and semimetals, respectively.

E_{xc}	Phase	SOI	E_{VBM}	k_{VBM}	E_{CBM}	k_{CBM}	E_{gap}^i	E_{gap}^d	k_{gap}^d	Type
LDA	Bi_2Te_3	X	−0.098	0.000 0.000 0.000	0.098	0.000 0.000 0.000	0.196	0.196	0.000 0.000 0.000	SC
		O	−0.055	0.140 0.000 0.500	0.056	0.130 0.000 0.500	0.111	0.115	0.130 0.000 0.500	SC
	Bi_4Te_5	X	0.027	0.040 0.040 0.500	−0.078	0.007 0.007 0.500	−0.105	0.017	0.007 0.007 0.500	SM
		O	−0.004	0.180 0.000 0.000	−0.028	0.090 0.000 0.000	−0.024	0.005	0.000 0.000 0.500	SM
	Bi_6Te_7	X	0.021	0.040 0.040 0.500	−0.057	0.020 0.000 0.000	−0.078	0.007	0.013 0.013 0.000	SM
		O	−0.009	0.000 0.000 0.000	−0.013	0.100 0.000 0.000	−0.004	0.006	0.010 0.000 0.000	SM
	Bi_8Te_9	X	−0.004	0.070 0.000 0.500	−0.019	0.013 0.013 0.500	−0.015	0.007	0.013 0.013 0.500	SM
		O	−0.005	0.000 0.000 0.000	−0.002	0.000 0.000 0.000	0.003	0.003	0.000 0.000 0.000	SC
	BiTe	X	0.024	0.060 0.000 0.000	−0.028	0.020 0.020 0.500	−0.052	0.013	0.060 0.000 0.000	SM
		O	−0.062	0.060 0.000 0.000	0.048	0.027 0.027 0.500	0.110	0.134	0.040 0.000 0.500	SC
	Bi_4Te_3	X	0.025	0.110 0.000 0.000	−0.039	0.027 0.027 0.500	−0.064	0.036	0.027 0.027 0.500	SM
		O	0.081	0.000 0.000 0.000	−0.077	0.500 0.000 0.000	−0.158	0.001	0.020 0.000 0.000	SM
	Bi_2Te	X	0.044	0.067 0.067 0.000	−0.083	0.033 0.033 0.000	−0.127	0.005	0.033 0.033 0.000	SM
		O	0.120	0.000 0.000 0.000	−0.045	0.500 0.000 0.500	−0.165	0.021	0.020 0.000 0.000	SM
	Bi_7Te_3	X	0.085	0.170 0.000 0.000	−0.068	0.033 0.033 0.500	−0.153	0.010	0.033 0.033 0.500	SM
		O	0.041	0.000 0.000 0.000	−0.095	0.500 0.000 0.500	−0.136	0.009	0.000 0.000 0.000	SM
	Bi_2	X	0.073	0.053 0.053 0.500	−0.207	0.500 0.000 0.500	−0.280	0.011	0.500 0.000 0.500	SM
		O	0.076	0.000 0.000 0.500	−0.038	0.500 0.000 0.500	−0.114	0.089	0.500 0.000 0.500	SM

PBE calculations give the electronic band structures shown in Figure 3. The band structure of Bi_2Te_3 is shown in Figure 3a. There is a VBM of -0.136 eV at Γ and a CBM of 0.136 at Γ, indicating that Bi_2Te_3 is a semiconductor as previously reported [31–33]. Note that the experimental energy gap is about 0.13 eV. Figure 3d shows that Bi_8Te_9 has a VBM of -0.004 eV on A$-$H (0.033, 0.033, 0.5), CBM of -0.03 eV on A$-$H (0.007, 0.007, 0.5), and E_{gap}^d of 0.027 eV on A$-$L (0.02, 0, 0.5). The band structure of BiTe in Figure 3e shows that VBM is 0.017 eV on $\Gamma-$M (0.06, 0, 0), CBM is -0.023 eV on A$-$H (0.013, 0.013, 0.5), and E_{gap}^d is 0.035 eV on $\Gamma-$M (0.06, 0, 0). The band structure of Bi_2 is shown in Figure 3i, where VBM is 0.066 eV on A$-$H (0.047, 0.047, 0.5), CBM is -0.197 eV on A$-$L (0.48, 0, 0.5), and E_{gap}^d is 0.02 eV on A$-$H (0.047, 0.047, 0.5). Note that our result for Bi_2 is consistent with the experimental reports that bulk Bi is semimetallic [34] since the supercell of Bi_2 is to be bulk Bi. Additionally, the other phases (Bi_4Te_5, Bi_6Te_7, Bi_4Te_3, Bi_2Te, Bi_7Te_3) were semimetallic, as shown in Figure 3 and Table 2. Note that PBE showed that the electric transport types of $(Bi_2)_m(Bi_2Te_3)_n$ were semimetallic because of positive E_{gap}^d and negative E_{gap}^i except for Bi_2Te_3. In addition, the electric transport types of $(Bi_2)_m(Bi_2Te_3)_n$ from LDA are the same as those from PBE, although the detailed values (E_{VBM}, k_{VBM}, E_{CBM}, k_{CBM}, E_{gap}^i, k_{gap}^i) of LDA were different from those of PBE (see Figures 3–5 and Tables 2 and 3).

Meanwhile, when considering the SOI in the PBE calculations, there are some changes in the band structures (see Figure 4 and Table 2). In our results, SOI flattens the electronic band of $(Bi_2)_m(Bi_2Te_3)_n$ in the vicinity of the band edges (VBM and CBM) because dE/dk decreases near these edges. We expect that this is related to the change in the electronic effective mass near the VBM and CBM, although it was not quantitatively analysed. For Bi_2Te_3, the SOI calculations accompanied an increase in the energy level of VBM (-0.061 eV) and a decrease in that of CBM (0.068 eV), resulting in a slight decrease in energy gaps ($E_{gap}^i = 0.129$ eV, $E_{gap}^d = 0.135$ eV). For Bi_2, the SOI calculation increases both VBM (0.113 eV) and CBM (-0.048 eV), leading to a small increase in the energy gap values ($E_{gap}^i = -0.161$ eV, $E_{gap}^d = 0.079$ eV). In addition, for BiTe, the SOI calculations decrease VBM (-0.064 eV) and increase CBM (0.053 eV), eventually opening E_{gap}^i (0.117 eV), unlike closed gaps from calculations without SOI (-0.04 eV). Note that the electric transport type of BiTe changes to a semiconductor of calculations with SOI unlike semimetals of the calculations without SOI. For the other phases except for BiTe, with SOI, the electric transport types do not change, although E_{VBM}, k_{VBM}, E_{CBM}, k_{CBM}, E_{gap}^i, and k_{gap}^i change slightly compared to the case without SOI. In addition, note that with SOI, LDA and PBE give the same electric transport types except for Bi_8Te_9 and BiTe unlike the results of the band structures from the calculations without SOI, although the detailed values (E_{VBM}, k_{VBM}, E_{CBM}, k_{CBM}, E_{gap}^i, and k_{gap}^i) changed (see Figures 4–6 and Tables 2 and 3). In detail, LDA with SOI changes the electric transport types of Bi_8Te_9 and BiTe from semimetals to semiconductors owing to the decrease in VBM (-0.005 eV for Bi_8Te_9, -0.062 eV for BiTe) and the increase in CBM (-0.002 eV for Bi_8Te_9, 0.048 eV for BiTe). Note that although it is not possible to explicitly state the semiconductor type, DFT calculations can determine possible electric transport types. Therefore, for the $(Bi_2)_m(Bi_2Te_3)_n$ homologous series, only three phases (Bi_2Te_3, Bi_8Te_9, BiTe) can be semiconductors.

4. Conclusions

First-principles DFT calculations of $(Bi_2)_m(Bi_2Te_3)_n$ were performed with fixed experimental lattice parameters to estimate their phase stabilities and to analyse the properties of the atomic structures and electronic band structures. For E_{xc}, PBE and LDA were considered with or without SOI. From the structural analysis, PBE overestimated the distances between adjacent atoms along the *c*-axis in the intralayers of $(Bi_2)_m(Bi_2Te_3)_n$ compared to LDA, and LDA overestimated the interlayer distances in $(Bi_2)_m(Bi_2Te_3)_n$ compared to PBE. From the electronic band structures, the electric transport types of $(Bi_2)_m(Bi_2Te_3)_n$ remained as semimetals or semiconductors regardless of whether the E_{xc} type or SOI was considered, except for Bi_8Te_9 and BiTe. Our calculations revealed that Bi_8Te_9, BiTe, and Bi_2Te_3 are expected to be semiconductors. Consequently, Bi_8Te_9 and BiTe, including the

well-known thermoelectric Bi_2Te_3, are expected to be potential thermoelectric materials for automobile energy harvesting technologies.

Author Contributions: S.P. (Sungjin Park) and B.R. conceived the idea. S.P. (Sungjin Park) performed all calculations. S.P. (Sungjin Park) and B.R. contributed to the discussion on the purposes of the manuscript. S.P. (SuDong Park) contributed to the discussion on the research direction and the manuscript. S.P. (Sungjin Park) wrote the manuscript with revision from the other authors. All authors have read and agreed to the published version of the manuscript.

Institutional Review Board Statement: Not applicable.

Informed Consent Statement: Not applicable.

Data Availability Statement: Not applicable.

Conflicts of Interest: The authors declare no conflict of interest.

Nomenclature

Acronym	Meaning
BL	bilayer
CBM	conduction band minimum
DFT	density functional theory
DOS	density of states
E_F	Fermi level
E_{Mixing}	layer mixing energy
E_{gap}^d	direct energy gap (bandgap)
E_{gap}^i	indirect energy gap (bandgap)
E_{VBM}	energy of valence band maximum
E_{CBM}	energy of conduction band minimum
E_{xc}	exchange–correlation functional
k_{gap}^d	reciprocal position of direct energy gap (bandgap)
k_{VBM}	reciprocal position of valence band maximum
k_{CBM}	reciprocal position of conduction band minimum
LDA	local density approximation
LDA + SOI	local density approximation with spin–orbit interaction
N_{Atom}	total number of atoms in the supercell
N_{BL}	the number of bilayers
N_{QL}	the number of quintuple layers
PAW	projector augmented wave
PBE	Perdew–Burke–Ernzerhof
PBE + SOI	Perdew–Burke–Ernzerhof with spin–orbit interaction
QL	quintuple layer
SC	semiconductor
SM	semimetal
SOI	spin–orbit interaction
VBM	valence band maximum

References

1. Hsu, C.; Yao, D.; Ye, K.; Yu, B. Renewable energy of waste heat recovery system for automobiles. *J. Renew. Sustain. Energy* **2010**, *2*, 013105. [CrossRef]
2. Yu, S.; Du, Q.; Diao, H.; Shu, G.; Jiao, K. Start-up modes of thermoelectric generator based on vehicle exhaust waste heat recovery. *Appl. Energy* **2015**, *138*, 276–290. [CrossRef]
3. Kim, S.; Park, S.; Kim, S.; Rhi, S. A thermoelectric generator using engine coolant for light-duty internal combustion engine-powered vehicles. *J. Electron. Mater.* **2011**, *40*, 812–816. [CrossRef]
4. Elsheikh, M.H.; Shnawah, D.A.; Sabri, M.F.M.; Said, S.B.M.; Hassan, M.H.; Bashir, M.B.A.; Mohamad, M. A review on thermoelectric renewable energy: Principle parameters that affect their performance. *Renew. Sustain. Energy Rev.* **2014**, *30*, 337–355. [CrossRef]
5. Orr, B.; Akbarzadeh, A.; Mochizuki, M.; Singh, R. A review of car waste heat recovery systems utilising thermoelectric generators and heat pipes. *Appl. Therm. Eng.* **2016**, *101*, 490–495. [CrossRef]
6. Enescu, D. Thermoelectric energy harvesting: Basic principles and applications. In *Green Energy Advances*; Enescu, D., Ed.; Open Access Peer-Reviewed Edited Vol.; IntechOpen Limited: London, UK, 2019. [CrossRef]
7. Hsiao, Y.Y.; Chang, W.C.; Chen, S.L. A mathematic model of thermoelectric module with applications on waste heat recovery from automobile engine. *Energy* **2010**, *35*, 1447–1454. [CrossRef]
8. Arnaud, L.; Ludovic, G.; Mouad, D.; Hamid, Z.; Vincent, L. Comparison and impact of waste heat recovery technologies on passenger car fuel consumption in a normalized driving cycle. *Energies* **2014**, *7*, 5273–5290. [CrossRef]
9. Ryu, B.; Chung, J.; Choi, E.; Ziolkowski, P.; Müller, E.; Park, S.D. Counterintuitive example on relation between ZT and thermoelectric efficiency. *Appl. Phys. Lett.* **2020**, *116*, 193903. [CrossRef]
10. Ryu, B.; Chung, J.; Park, S.D. Thermoelectric degrees of freedom determining thermoelectric efficiency. *iScience* **2021**, *24*, 102934. [CrossRef]
11. Selvan, K.V.; Ali, M.S.M. Micro-scale energy harvesting devices: Review of methodological performances in the last decade. *Renew. Sustain. Energy Rev.* **2016**, *54*, 1035–1047. [CrossRef]
12. Mamur, H.; Bhuiyan, M.R.A.; Korkmaz, F.; Nil, M. A review on bismuth telluride (Bi2Te3) nanostructure for thermoelectric applications. *Renew. Sustain. Energy Rev.* **2018**, *82*, 4159–4169. [CrossRef]
13. Burkov, A.T. Silicide thermoelectrics: Materials for energy harvesting. *Phys. Status Solidi A* **2018**, *215*, 1800105. [CrossRef]
14. Bos, J.W.G.; Zandbergen, H.W.; Lee, M.-H.; Ong, N.P.; Cava, R.J. Structures and thermoelectric properties of the infinitely adaptive series $(Bi_2)_m(Bi_2Te_3)_n$. *Phys. Rev. B* **2007**, *75*, 195203. [CrossRef]
15. Bos, J.W.G.; Faucheux, F.; Downie, R.A.; Marcinkova, A. Phase stability, structures and properties of the $(Bi_2)_m$ $(Bi_2Te_3)_n$ natural superlattices. *J. Solid State Chem.* **2012**, *193*, 13–18. [CrossRef]
16. Kuznetsov, P.I.; Yapaskurt, V.O.; Shchamkhalova, B.S.; Shcherbakov, V.D.; Yakushcheva, G.G.; Luzanov, V.A.; Jitov, V.A. Growth of Bi_2Te_3 films and other phases of Bi-Te system by MOVPE. *J. Cryst. Growth* **2016**, *455*, 122–128. [CrossRef]
17. Mao, C.; Tan, M.; Zhang, L.; Wu, D.; Bai, W.; Liu, L. Experimental reinvestigation and thermodynamic description of Bi-Te binary system. *Calphad* **2018**, *60*, 81–89. [CrossRef]
18. Zhu, H.Z.; Zhao, C.; Nan, P.; Jiang, X.; Zhao, J.; Ge, B.; Xiao, C.; Xie, Y. Intrinsically low lattice thermal conductivity in natural superlattice $(Bi_2)_m(Bi_2Te_3)_n$ thermoelectric materials. *Chem. Mater.* **2021**, *33*, 1140–1148. [CrossRef]
19. Hohenberg, P.; Kohn, W. Inhomogeneous electron gas. *Phys. Rev.* **1964**, *136*, B864. [CrossRef]
20. Kohn, W.; Sham, L.J. Self-consistent equations including exchange and correlation effects. *Phys. Rev.* **1965**, *140*, A1133. [CrossRef]
21. Kresse, G.; Hafner, J. Ab initio molecular dynamics for liquid metals. *Phys. Rev. B* **1993**, *47*, 558. [CrossRef]
22. Kresse, G.; Hafner, J. Ab initio molecular-dynamics simulation of the liquid-metal–amorphous-semiconductor transition in germanium. *Phys. Rev. B* **1994**, *49*, 14251. [CrossRef] [PubMed]
23. Hafner, J. Ab-initio simulations of materials using VASP: Density-functional theory and beyond. *J. Comput. Chem.* **2008**, *29*, 2044–2078. [CrossRef] [PubMed]
24. Perdew, J.P.; Burke, K.; Ernzerhof, M. Generalized gradient approximation made simple. *Phys. Rev. Lett.* **1996**, *77*, 3865. [CrossRef]
25. Blöchl, P.E. Projector augmented-wave method. *Phys. Rev. B* **1994**, *50*, 17953. [CrossRef] [PubMed]
26. Kresse, G.; Joubert, D. From ultrasoft pseudopotentials to the projector augmented-wave method. *Phys. Rev. B* **1999**, *59*, 1758. [CrossRef]
27. Kaupp, M.; Malkina, O.L.; Malkin, V.G.; Pyykkö, P. How do spin–orbit-induced heavy-atom effects on NMR chemical shifts function? Validation of a simple analogy to spin–spin coupling by density functional theory (DFT) calculations on some iodo compounds. *Chem. Eur. J.* **1998**, *4*, 118–126. [CrossRef]
28. Autschbach, J.; Ziegler, T. Nuclear spin–spin coupling constants from regular approximate relativistic density functional calculations. I. Formalism and scalar relativistic results for heavy metal compounds. *J. Chem. Phys.* **2000**, *113*, 936. [CrossRef]
29. Autschbach, J.; Ziegler, T. Nuclear spin–spin coupling constants from regular approximate relativistic density functional calculations. II. Spin–orbit coupling effects and anisotropies. *J. Chem. Phys.* **2000**, *113*, 9410. [CrossRef]
30. Ong, S.P.; Richards, W.D.; Jain, A.; Hautier, G.; Kocher, M.; Cholia, S.; Gunter, D.; Chevrier, V.; Persson, K.A.; Ceder, G. Python materials genomics (pymatgen): A robust, open-source python library for materials analysis. *Comput. Mater. Sci.* **2013**, *68*, 314–319. [CrossRef]
31. Goldsmid, H. Recent studies of bismuth telluride and its alloys. *J. Appl. Phys.* **1961**, *32*, 2198. [CrossRef]

32. Thomas, G.; Rapkine, D.; Van Dover, R.; Mattheiss, L.; Sunder, W.; Schneemeyer, L.; Waszczak, J. Large electronic-density increase on cooling a layered metal: Doped Bi_2Te_3. *Phys. Rev. B* **1992**, *46*, 1553. [CrossRef] [PubMed]

33. Park, S.; Ryu, B. Hybrid-density functional theory study on the band structures of tetradymite-Bi_2Te_3, Sb_2Te_3, Bi_2Se_3, and Sb_2Se_3 thermoelectric materials. *J. Korean Phys. Soc.* **2016**, *69*, 1683–1687. [CrossRef]

34. Lannin, J.; Calleja, J.; Cardona, M. Second-order Raman scattering in the group-Vb semimetals: Bi, Sb, and As. *Phys. Rev. B* **1975**, *12*, 585. [CrossRef]